Journal of Applied Fluid Mechanics, Vol. 16, No. 9, pp. 1767-1777, 2023.
Available online at www.jafmonline.net, ISSN 1735-3572, EISSN 1735-3645.
https://doi.org/10.47176/jafm.16.09.1672

Experimental Study of Secondary Flow in Narrow and Sharp Open-Channel Bends

P. Hu and M. Yu†

State Key Laboratory of Water Resources and Hydropower Engineering, Wuhan University, Wuhan 430072, China

†*Corresponding author Email: mhyu@whu.edu.cn*

ABSTRACT

Secondary flow is a prominent feature of channel bends; it alters the streamwise velocity and bed shear stress distributions. Experiments were conducted to investigate the complex pattern of secondary flow in a narrow and sharp open-channel bend and the underlying mechanism of generation of multiple circulation cells. Compared with the moderate bends, the sharp bends are characteristic of multiple circulation cells from the 90° section. In addition to the curvature-induced circulation cell (S1) and turbulence-induced counter-rotation circulation cell (C1) near the outer bank, another circulation cell (S2) was observed near the inner bank and was attributed to flow separation. A term-by-term analysis of the vorticity equations indicates that the centrifugal term favours S1 and C1 while opposing S2. The turbulence-related term accounts for the formation of C1 and S2. The advective transport term redistributes vorticity and maintains the existence of S2. The dependence of secondary flow structure on Reynolds number and aspect ratio was also explored. With an increase in the Reynolds number from 23000 to 37000, both the strength and size of C1 are reduced by 50%, whereas the size of S2 increases by 20%, and its strength slightly decreases. With a decrease in the aspect ratio from 3.3 to 2, the strengths of S1, S2, and C1 are doubled, and the sizes of C1 and S2 increase by 90% and 20%, respectively.

Article History

Received November 19, 2022
Revised April 18, 2023
Accepted April 19, 2023
Available online July 1, 2023

Keywords:

Secondary flow
Vorticity transport equations
Open-channel bends
Aspect ratio
Reynolds number

1. INTRODUCTION

The flow is subject to a helical pattern in open-channel bends (Kashyap et al., 2012). Secondary flow, which is the flow component perpendicular to the channel axis, redistributes the velocity and boundary shear stress. Since the 1860s, curvature-induced secondary flow has been extensively investigated using field and laboratory measurements and numerical simulations (Bathurst et al., 1977; Blanckaert & De Vriend, 2004; Khosronejad et al., 2007; Nanson, 2010; Constantinescu et al., 2013). It is classified as a secondary flow of Prandtl's first kind (Prandtl, 1942) that is formed by two counteracting mechanisms: the centrifugal acceleration and centripetal pressure gradient arisen from the transvers water surface slope (Stoesser et al., 2010, Blanckaert et al., 2012), resulting in the opposite flow direction in the upper and lower parts. Secondary flow plays an important role in river morphology. Thomson (1876) linked the propensity of sediment transport from the outer to inner banks to secondary flow. Hooke (1975), Ruether and Olsen (2005), and Feurich and Olsen (2011) reported the phenomenon of sediment erosion on the outer bank and deposition on the inner bank of the bend.

In addition to the curvature-induced second secondary flow, a weaker counter-rotating circulation has often been observed in the outer bank in both laboratory and field experiments (Bathurst et al., 1979, Blanckaert & De Vriend, 2004, Farhadi et al., 2018). Van Balen et al. (2009) investigated the outer bank circulation cell using large-eddy simulation and concluded that it evolved from both the centrifugal force and anisotropy of turbulence. Blanckaert and De Vriend (2004) conducted detailed laboratory experiments and suggested that the generation of the outer bank cell is related to the transformation of kinetic energy from time-averaged to turbulent flow. Therefore, it is often classified as a secondary flow of Prandtl's second kind, generated by turbulence (Prandtl, 1942). Stoesser et al. (2010) compared the simulation results between the LES and isotropic Reynolds averaged Navier-Stokes (RANS) models and found that

Nomenclature

B	channel width	T_{ani}	term associated with the Reynolds normal stresses
Fr	Froude number	T_{rss}	term associated with the Reynolds shear stresses
H	water depth	T_{dif}	dissipation term
p	pressure	U	overall mean velocity
Q	discharge	u_i'	fluctuating velocity
R	radius of curvature of the channel axis	u_θ	streamwise velocity
Re	Reynolds number	u_r	transverse velocity
S	bed slope	u_z	vertical velocity
t	time	θ , r, z	cylindrical coordinate system
T_{adv}	transport term in the vorticity equation	ν	molecular kinematic viscosity
T_{cur}	curvature-related term	w_θ	streamwise vorticity
T_{cf} , T_{cf1} , T_{cf2}	centrifugal terms		

the isotropic model was unable to predict the existence of the circulation cell, which also indicates that turbulence anisotropy is key in the formation of the circulation cell. In addition, the existence of positive feedback between centrifugal forces and the outer bank circulation cell intensifies the complexity. However, the influence of this circulation on bank stability remains controversial. Bathurst et al. (1979) hypothesised that the circulation cell endangers the outer bank stability, as the high-momentum fluid is diverted downwards. Blanckaert and De Vriend (2004) argued that the circulation cell has a positive effect on bank stability because a buffer layer is formed that protects the bank from the influence of primary circulation cell.

Blanckaert and De Vriend (2010) reported that $C_f^{-1}H/B$ and R/B are the prevailing parameters that influence secondary flow, where H is the water depth and C_f is the Chezy friction factor. The former reflects the combined effect of bed roughness and channel shallowness, and the latter represents the curvature ratio. Bend sharpness is represented by the ratio of the radius of curvature of the channel centreline R to the channel width B. For mildly curved bends, the value of R/B has an order of magnitude of O (10) or larger. For sharp bends, the value is smaller than 3 (Crosato, 2008). In mildly curved channels, the interactions between the streamwise velocities and secondary flow are negligible. Johannesson and Parker (1989) adopted a logarithmic profile of streamwise velocities and proposed an analytical solution for secondary flow. A decrease in the curvature ratio often results in an increase in the circulation strength. Previous studies have indicated that the flow characteristics of sharp bends differed from the moderate curvature bends (Blanckaert, 2011; Hu et al., 2019). Pronounced flow separation in the inner bank region often occurs in sharp bends. A shear layer exists near the edge of flow separation zone with enhanced streamwise velocity gradients, turbulent kinetic energy, and Reynolds shear stresses (Blanckaert, 2015). Despite the engineering significance, little is known about the effect of flow separation on secondary flow.

The flow behaviour in open-channel bends is considerably sensitive to the channel geometry. Yan et al. (2020) found that the size, strength and location of circulation cells varied with the bank slope. The aspect ratio B/H also influences the secondary flow structure and bend migration rate (Russell & Vennell, 2019). Secondary flow patterns in relatively wide and shallow channel bends (B/H > 10) have been extensively studied (Dietrich & Smith, 1983). Van Balen et al. (2010) found that with increase of H, the strength of the outer bank circulation cell increases in the upstream part, whereas it decreases in the downstream part. Nanson (2010) indicated that the flow and corresponding morphology characteristics in narrow and deep bends significantly differ from those in wide and shallow bends because the effect of bed friction is limited in narrow deep channels, compared with bank friction. The Froude and Reynolds numbers are dominant parameters in open-channel flow (Wei et al., 2016). Farhadi et al. (2018) found that an increase in the Froude number causes the extension of the main circulation cell over larger areas of section, whereas the outer bank circulation cell is pushed towards the boundaries. Mahmoodi et al. (2021) found that an increase in Reynolds number results in an increase in normal-stress differences, which enhances the centrifugal force.

Investigation of the secondary flow structure helps optimise bank protection alternatives, design measures for environmental improvement, and reduce adverse impacts in hydraulic and environmental engineering problems (Kang et al., 2018, Abduo et al., 2021). Although extensive work has been conducted, the mechanism leading to complex secondary flow remains unclear, particularly with respect to sharp and narrow open-channel bends. The objectives of this study are to (1) investigate the secondary flow structure in narrow and sharp open-channel bends, (2) explore the underlying mechanism of the generation of multiple circulation cells by analysing terms in streamwise vorticity equation, and (3) investigate the dependence of all circulation cells on the channel aspect ratio and Reynolds number.

Table 1 Geometric and hydraulic conditions

Cases	*Q* (L/s)	*R* (m)	*B* (m)	*H* (m)	*U* (m/s)	*S* (%)	*Re* (10^4)	*B/H*	*Fr*
1	9	1.2	0.4	0.15	0.15	0.08	2.3	2.7	0.12
2	12	1.2	0.4	0.15	0.2	0.08	3	2.7	0.16
3	15	1.2	0.4	0.15	0.25	0.08	3.7	2.7	0.21
4	12	1.2	0.4	0.2	0.15	0.08	3	2.0	0.11
5	12	1.2	0.4	0.12	0.25	0.08	3	3.3	0.23

2. EXPERIMENTS AND DATA COLLECTION

Experiments were conducted in a plexiglass laboratory flume. The planar structure of the flume is shown in Fig. 1(a). The straight inflow and outflow reaches are 3.5 m and were joined to a 180° bend. The plane configuration was based on the middle reaches of Jinghe River located in the Loess Plateau in China. The scale of the test is 1:300, the width of the channel and the depth of the laboratory is determined according the actual landform. This plane configuration (180° single bend) was also adopted by Van Balen et al. (2009), Luo and Razinsky (2009), Bai et al. (2014), Vaghefi et al. (2016). The curvature ratio(R/B) of the natural river ranges from 2.5-3.5, and a constant curvature ratio was adopted (R/B=3). The constant radius of curvature is 1.2 m, and the flume width is 0.4 m. With a curvature ratio of 3, this flume falls within the range of natural rivers with sharp curvatures. As we known that the Froude number reflect the ratio of the inertia force to the gravity force, and the Froude similarity criterion is the most important similarity criterion that guarantees the similarity between the model and the prototype of natural rivers. Then, the discharge is determined according to the Froude similarity criterion. The discharge ranges from 9-15L/s, and the Fr ranges from 0.11-0.23, which is consistent with the actual situation (Hu et al., 2019). The constant radius of curvature is 1.2 m, and the flume width is 0.4 m. With a curvature ratio of 3, this flume falls within the range of natural rivers with sharp curvatures. The experiments were conducted with plane bed to avert the influences of channel morphology.

Table 1 lists the hydraulic conditions for the five cases. For Cases 1, 2, and 3, H is constant. The aspect ratio is constant for these three cases, and the Re ranges from 23000 to 37000 with the variation of discharge. For Cases 2, 4, and 5, the discharge is constant. The Re is constant for these three cases and the aspect ratio ranges from 2.0 to 3.3 with the variation of water depth. These settings allow us to investigate the flow processes for different Reynolds numbers and aspect ratios. The flow regimes were turbulent and subcritical.

During the experiment, the discharge in the circulating water system was unchanged. The discharge measurements were performed using a calibrated flow meter. The water surface level at the exit was controlled using a needle water level gauge. The water volume was changed to achieve different water surface levels for Cases 2, 4, and 5. Grilles were used for energy dissipation at the bend entrance. After the flow was stabilised, three-dimensional velocity vectors were measured using an

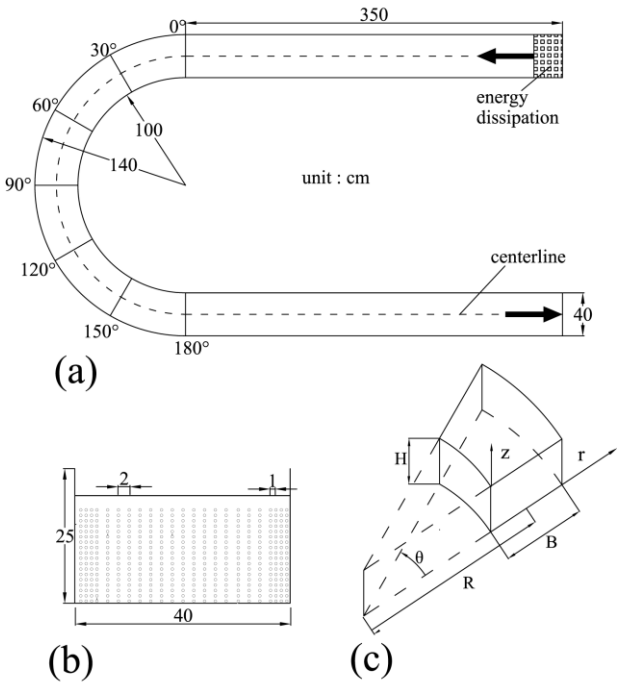

Fig. 1. Experimental set-up: (a) plan view of the laboratory flume; (b) measuring grid; (c) coordinate system.

Acoustic Doppler Velocimeter (ADV). ADV was fixed on a facility which can move up, down, left and right. The receivers of ADV were parallel to the primary flow direction. The measured instantaneous velocity series were used to calculated the time-averaged velocities, fluctuating velocities, and Reynolds stresses. The combined use of a side-looking probe and down-looking probe made it possible to measure the near boundary region. The sampling frequency and acquisition time were set to 200 Hz and 60 s. Seven sections (0°, 30°, 60°, 90°, 120°, 150°, and 180°) were measured. The measurement grid is illustrated in Fig. 1(b). Each section includes 23 measurement lines. The vertical spacing is 1 cm. The data were analysed using a cylindrical coordinate system (Fig. 1(c)). The θ axis pointed downstream, the r axis was perpendicular to the θ axis and pointed outwards, and the z axis was in a vertical position, pointing upwards.

3. THEORY CONSIDERATION

Cross-stream motion is reflected in the momentum equations. The continuity equation and transverse and vertical momentum equations of fluid flow in cylindrical

polar coordinates are as follows (Dey, 2014):

$$\frac{\partial u_r}{\partial r}+\frac{1}{r}\frac{\partial u_r}{\partial \theta}+\frac{\partial u_r}{\partial z}+\frac{u_r}{r}=0 \quad \cdots\cdots\cdots\cdots\cdots\cdots \quad \cdots\cdots(1)$$

$$\frac{\partial u_r}{\partial t}+u_r\frac{\partial u_r}{\partial r}+\frac{u_\theta}{r}\frac{\partial u_r}{\partial \theta}+u_z\frac{\partial u_r}{\partial z}-\frac{u_\theta^{\,2}}{r}= -\frac{\partial p}{\partial r}+\nu\left(\nabla^2 u_r-\frac{u_r}{r^2}-\frac{2}{r^2}\frac{\partial u_\theta}{\partial \theta}\right) \quad \cdots\cdots\cdots\cdots\cdots\cdots(2)$$

$$\frac{\partial u_z}{\partial t}+u_r\frac{\partial u_z}{\partial r}+\frac{u_\theta}{r}\frac{\partial u_z}{\partial \theta}+u_z\frac{\partial u_z}{\partial z}=-\frac{\partial p}{\partial z}+\nu\nabla^2 u_r \quad (3)$$

where t is the time, $u_\theta$is the streamwise velocity, $u_r$is the transverse velocity, u_z is the vertical velocity, ν is the molecular kinematic viscosity, and p is pressure, ∇^2 is the Laplace operator.

In turbulent flow, hydrodynamic quantities fluctuate irregularly in time. The instantaneous velocity components are expressed as:

$$u_i=\overline{u_i}+u_i'\ (i=r,\theta,z) \quad (4)$$

where $\overline{u_i}$ is the time-averaged velocity (the superscript is omitted for brevity), and u_i' is the fluctuating velocity.

The vorticity equations reveal the driving and dissipating of circulation cells. Streamwise vorticity w_θ is defined as follows:

$$w_\theta=\frac{\partial u_z}{\partial r}-\frac{\partial u_r}{\partial z} \quad (5)$$

By cross-differentiation of Eqs. (2) and (3), the pressure term was counteracted. The streamwise vorticity equation is obtained as follows:

$$\begin{aligned}\frac{\partial w_\theta}{\partial t}=&-\left(\frac{u_\theta}{r}\frac{\partial w_\theta}{\partial \theta}+u_r\frac{\partial w_\theta}{\partial r}+u_z\frac{\partial w_\theta}{\partial z}\right)\\&-\left[\frac{\partial u_z}{\partial \theta}\frac{\partial}{\partial r}\left(\frac{u_\theta}{r}\right)-\frac{\partial u_r}{\partial \theta}\frac{\partial}{\partial z}\left(\frac{u_\theta}{r}\right)\right]\\&-\left(\frac{\partial u_r}{\partial r}w_\theta+\frac{\partial u_z}{\partial z}w_\theta\right)-\left[\frac{\partial}{\partial z}\left(\frac{u_\theta^{\,2}}{r}\right)+\frac{\partial}{\partial z}\left(\frac{\overline{u_\theta'^2}}{r}\right)\right]\\&+\frac{\partial^2}{\partial z\partial r}\left(\overline{u_r'^2}-\overline{u_z'^2}\right)+\frac{1}{r}\frac{\partial \overline{u_r'^2}}{\partial z}\\&+\frac{\partial^2 \overline{u_r'u_z'}}{\partial z^2}-\frac{\partial^2 \overline{u_r'u_z'}}{\partial r^2}-\frac{\partial}{\partial r}\left(\frac{\overline{u_r'u_z'}}{r}\right)\\&+\frac{\partial^2}{\partial\theta\partial z}\frac{\overline{u_\theta'u_r'}}{r}-\frac{\partial^2}{\partial\theta\partial r}\frac{\overline{u_\theta'u_z'}}{r}+\nu\left(\nabla^2 w_\theta+\frac{2}{r^2}\frac{\partial w_r}{\partial\theta}-\frac{w_\theta}{r^2}\right)\end{aligned} \quad (6)$$

The first term on Line 3 of Eq. (6) is transformed using Eq. (1):

$$\frac{\partial u_r}{\partial r}w_\theta+\frac{\partial u_z}{\partial z}w_\theta=-\left(\frac{1}{r}\frac{\partial u_r}{\partial\theta}+\frac{u_r}{r}\right)w_\theta \quad \cdots\cdots\cdots\cdots\cdots\cdots(7)$$

The gradients in θ direction were neglected, as these gradients were small and negligible. Eq. (6) can be simplified to:

$$\frac{\partial w_\theta}{\partial t}=T_{adv}+T_{cur}+T_{cf}+T_{ani}+T_{rss}+T_{dif} \quad (8)$$

$$\begin{aligned}T_{adv}&=-u_r\frac{\partial w_\theta}{\partial r}-u_z\frac{\partial w_\theta}{\partial z}\\T_{cur}&=\frac{u_r}{r}w_\theta\\T_{cf}&=T_{cf1}+T_{cf2}=-\frac{\partial}{\partial z}\left(\frac{u_\theta^{\,2}}{r}\right)-\frac{\partial}{\partial z}\left(\frac{\overline{u_\theta'^2}}{r}\right)\\T_{ani}&=\frac{\partial^2}{\partial z\partial r}\left(\overline{u_r'^2}-\overline{u_z'^2}\right)+\frac{1}{r}\frac{\partial \overline{u_r'^2}}{\partial z}\\T_{rss}&=\frac{\partial^2 \overline{u_r'u_z'}}{\partial z^2}-\frac{\partial^2 \overline{u_r'u_z'}}{\partial r^2}-\frac{\partial}{\partial r}\left(\frac{\overline{u_r'u_z'}}{r}\right)\\T_{dif}&=\nu\left(\nabla^2 w_\theta+\frac{2}{r^2}\frac{\partial w_r}{\partial\theta}-\frac{w_\theta}{r^2}\right)\end{aligned} \quad (9)$$

where T_{adv} is the advective transport of vorticity, T_{cf} and T_{cur}represent the influences of the centrifugal force and curvature, respectively, T_{cf1} and T_{cf2} represent the centrifugal force terms associated with the time-averaged and turbulence flow, respectively, T_{ani} and T_{rss} represent the influences of Reynolds normal and shear stresses, respectively, and T_{dif} represents the molecular viscosity dissipation, which was neglected in the present investigations (Hu et al., 2019). The variation of $\overline{u_r'^2}-\overline{u_z'^2}$ reflects the anisotropy of turbulence and variation of $\overline{u_r'u_z'}$ reflects the inhomogeneity of turbulence.

4. RESULTS AND DISCUSSIONS

4.1 Secondary Flow Structure Around the Bend

Secondary flow is the most important feature of an open-channel bend. With the development of flow, the pattern varied along the bend. In order to analyse it in detail, the normalised vectors of the cross-stream velocity components and normalised streamwise vorticity $w_\theta H/U$ in different sections of Case 4 are shown in Fig. 2.

At the 0° section, no circulation is evident. At the 30° section, one clockwise primary circulation cell (S1) is present which occupied almost the section. At the 60° section, apart from S1, a counter-clockwise rotating circulation cell (C1) near the outer bank is observed. S1 occupied most part of the section and is much larger than C1. Multiple circulation cells are observed from the 90° to the 150° sections. The primary circulation cell has an apparent split into two clockwise circulation cells (S1 and S2). S2 is formed close to the inner bank and is comparable in size to S1. Meanwhile, the size of C1 increases. Compared with the experiments in a wide and shallow bend (Van Balen et al., 2009), C1 is not constrained to the proximity of the outer bank and extends to the centre part of the cross-secton. The size of C1 is comparable to that of S1 in the 120° section. In the 180° section, S2 and C1 vanish, whereas S1 still exists. In accordance with the numerical results of Kashyap *et al.* (2012), two clockwise-rotating circulation cells exists in sharp bends. However, the core of S1 seems to locate closer to the outer bank due to the deformed bed topography. The aspect ratios range from 5 to 12.5, which are significantly larger than that of our experiments. C1 only appears in the simulations with R/B >8 and is restricted to the corner of the outer bank. The size of C1 is smaller than that of our

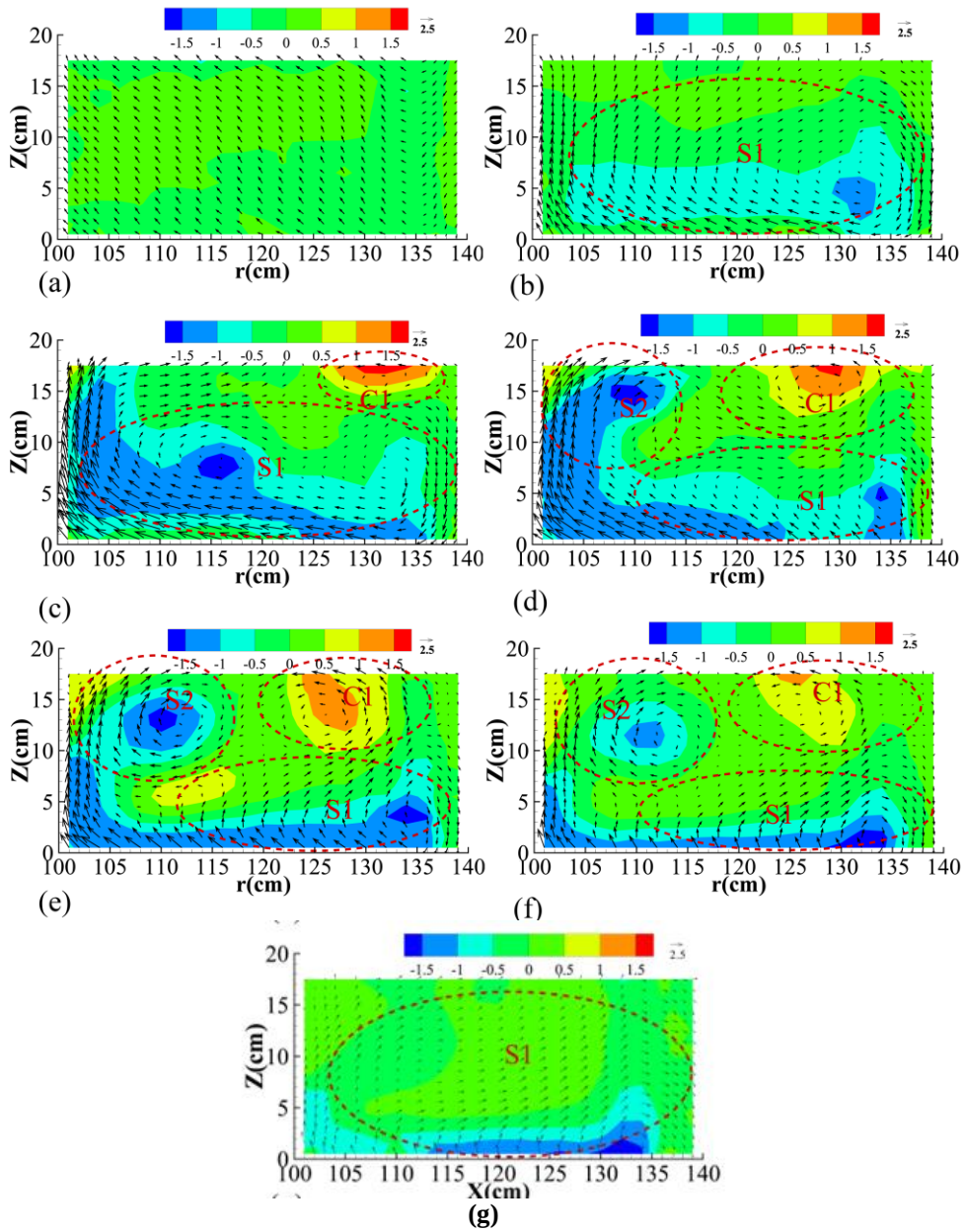

Fig. 2. Vectors of the velocity components and normalized vorticity distribution: (a) 0°; (b) 30°; (c) 60°; (d) 90°; (e) 120°; (f) 150°; (g) 180°. The red dashed lines denote the range of circulation cells.

experiments.

Streamwise vorticity is often used to visualise and quantify the complex secondary flow structure because the strength and rotation of circulation cells are clearly reflected. The mechanisms are also revealed by the streamwise vorticity equation. The normalised streamwise vorticity distribution is illustrated in Fig. 2. A negative value donates clockwise rotation, and a positive value donates counter-clockwise rotation. The zone of C1 is occupied by positive values, whereas the zones of S1 and S2 are occupied by negative values. C1 is clearly separated by the 0-isoline from S1 and S2. A transitional zone between S1 and S2 with reversed streamwise vorticity $w_\theta > 0$ exists. The normalised streamwise vorticity at the core of the circulation cells reflects the circulation strength, as shown in Fig. 3. The strengths of both C1 and S1 increase from the bend entrance to the 90° section, and

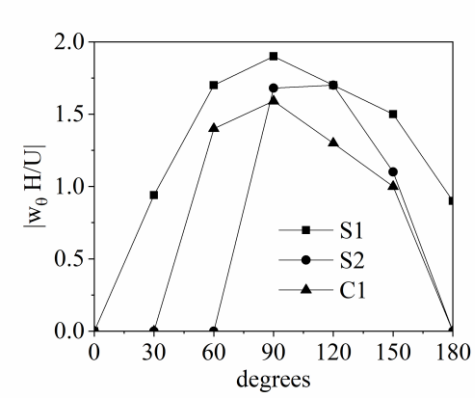

Fig. 3. Streamwise variation of the strength of the circulation cells.

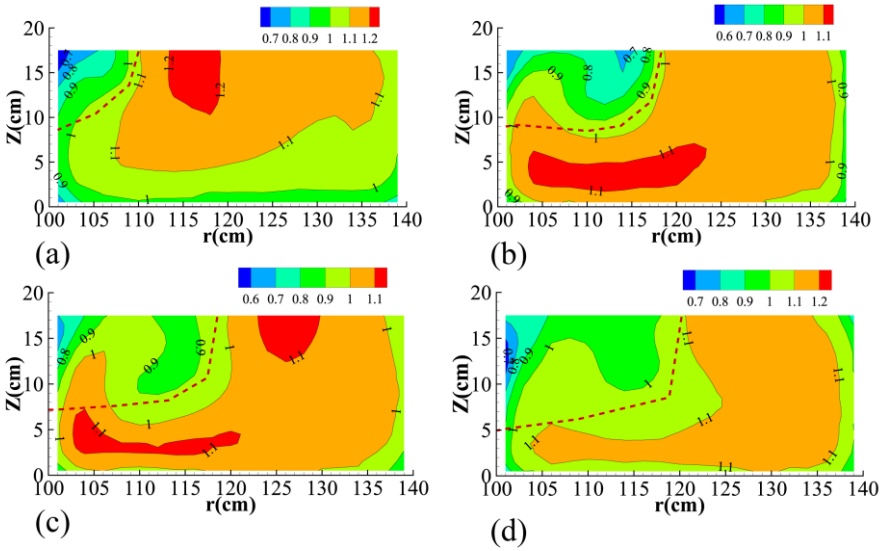

Fig. 4. Normalized streamwise velocity distribution: (a) 60°; (b) 90°; (c) 120°; (d) 150°. The red dashed lines denote the edge of flow separation.

then gradually decrease towards the end. S2 reaches its maximum strength at the 120° section and disappears at the 180° section.

The presence of S2, which is absent in mild-curvature bends, near the inner bank is related to flow separation. Owing to inertia, a sudden change in curvature in the bend entrance results in the flow cannot adjust rapidly enough to fit the inner bank. The flow appears to follow a straight path (Constantinescu et al., 2011). The normalised streamwise velocity patterns at the 60°, 90°, 120°, and 150° sections are plotted in Fig. 4. It is clear that the maximum velocities zone locates a certain distance from the inner bank, and a flow separation zone with substantially low velocities evolves. An internal shear layer was identified. From Figure 4, the flow separation zone was estimated according to the transverse profile of streamwise velocity. The inflexion points with steepest gradient determine the location of the internal shear layer. The flow separation zone narrows from the surface to bed. At the 0°section, the flow accelerates in the inner bank and decelerates in the outer bank. The inward mass transport opposes the flow separation, which occurs further downstream of the bend entrance, which complies with Blanckaert et al. (2015). Blanckaert (2015) clarified that the occurrence of flow separation mainly due to the spatial lag of inward pressure gradient force to outward inertial forces. The flow separation zone widens from the 60° to 150 sections. S2 corresponds to the flow separation zone. The size of S2 also starts growing in the 120° and 150° sections. The edge of flow separation seems to separate S2 from S1 and C1, indicating that the formation of S2 is closely related to the inner shear layer.

4.2 Terms of Vorticity Transport Equation

To gain insight into the mechanisms underlying complex secondary flow**,** terms of the vorticity transport equation at the 120° section were estimated based on the measured data. All terms were normalised by $(H/U)^2$ and are plotted in Fig. 5. The positive or negative values of the terms represent the tendency to increase or decrease the local vorticity, respectively. The order-of-magnitude analysis determined the main factors that influence the secondary flow pattern.

Figures 5(a) and (b) show the normalised distribution of centrifugal terms T_{cf1} and T_{cf2}, which are considered to be the generation of vorticity. T_{cf1} shows an order of magnitude larger than T_{cf2}. The zone with negative values corresponds to S1, indicating that T_{cf1}plays a crucial role in the existence of S1. However, patches of positive values can be seen in the upper corner of the inner banks, indicating thatT_{cf1} does not favour S2. The value of T_{cf1} is small within the C1 zone, and positive and negative variations indicate the complex effect of the centrifugal force on C1. The centrifugal term is correlated with the velocity gradient. As shown in Fig. 4, the distorted profile of streamwise velocity is prominent in the inner bank, with low values within the flow separation zone and high values near the bed. The adverse velocity gradient in the vertical direction causes a positive value of T_{cf1}in the flow separation zone.

Figures 5(c) and (d) show the transport T_{adv} and curvature-related T_{cur} terms. T_{cur} shows an order of magnitude smaller than T_{adv} and is neglectable. T_{adv} is of the same order of magnitude as T_{cf1}. T_{adv} redistributes the vorticity in the cross-section, and does not account for the generation or dissipation of vorticity. Large patches of the negative value of T_{adv} are located in the zone of S2, which balances T_{cf1}. After the formation of S2 in the 60° section, T_{adv} plays an important role in maintaining it.

Figures 5(e) and (f) provide normalized values of the terms associated with the Reynolds normal T_{ani} and shear T_{rss} stresses, which reflect the anisotropy and inhomogeneity of turbulence, respectively. T_{ani} and T_{rss} both show positive values in the zone of C1, which accounts for the formation of C1. Blankert and De Vriend (2004) suggested that C1 belongs to the secondary flow of Prandtl's second kind, associated with vorticity generated by the Reynolds stress tensor. On the contrary,

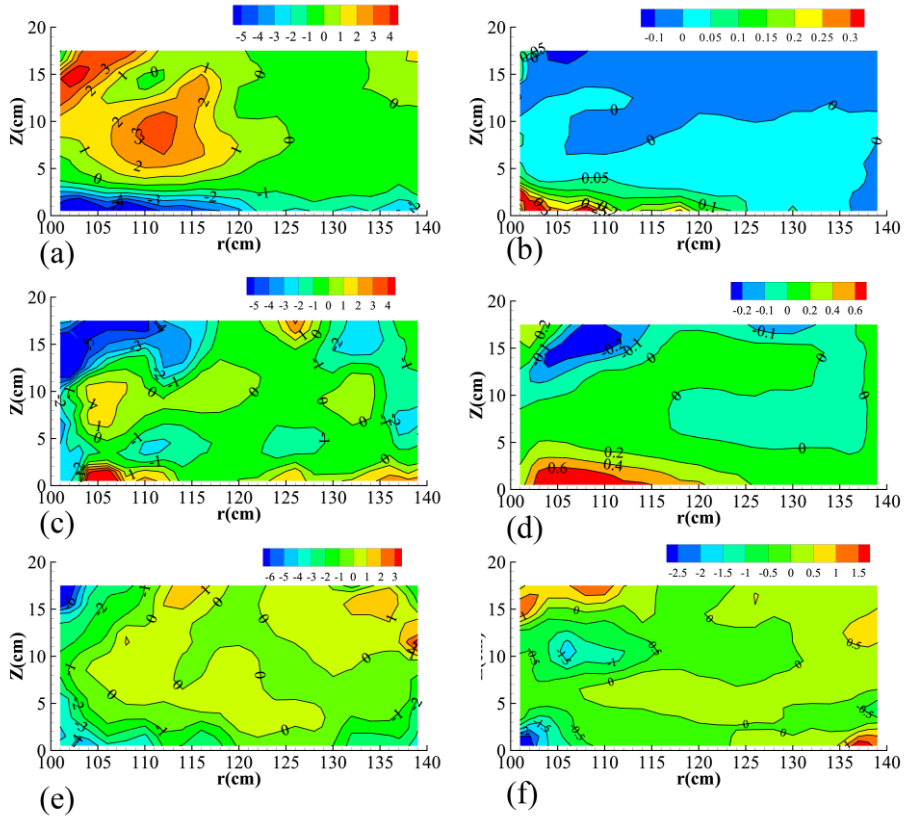

Fig. 5. Isolines of normalized terms in the vorticity equation at the 120° section, multiplied by 10: (a) T_{cf1}; (b) T_{cf2}; (c) T_{adv}; (d) T_{cur}; (e) T_{ani}; (f) T_{rss}.

Table 2 Variation of size and strength of the circulation cells with *Re*.

Cases	Re (10^4)	L_c			$\lvert w_\theta H/U \rvert$		
		S1	S2	C1	S1	S2	C1
1	2.3	0.63	0.47	0.42	1.10	0.82	0.84
2	3.0	0.65	0.49	0.35	1.15	0.8	0.65
3	3.7	0.65	0.61	0.22	1.15	0.78	0.48

large patches of negative values of T_{ani} and T_{rss} appear in the zone of S2. S2 can be referred to as turbulence-induced secondary flow. Within the range of S1, T_{ani} shows a negative value, which favours S1, whereas T_{rss} shows a positive value near the bed, which opposes S1. T_{rss} is smaller than T_{ani} but not negligible.

In summary, the transport, centrifugal, and turbulence terms play leading roles in determining the secondary flow pattern. Regarding streamwise vorticity equilibrium, the turbulence term is not purely dissipative. T_{cf1} favours S1 and C1 but opposes S2. T_{ani} and T_{rss} account for the formation of C1 and S2. T_{adv} redistributes the vorticity and maintains the existence of S2. Compared with the investigation on the outer bank circulation cell by Farhadi et al. (2018), the influence of the T_{rss} was emphasized. They found that the balance of vorticity is only discernible between T_{ani} and T_{cf1}.However, the Reynolds number in our experiment is larger than that in Farhadi's experiments. With the increase of Reynolds number, the inhomogeneity of turbulence increases and the role of the Reynolds shear stress enhances. The results that T_{rss} and T_{rss} behave differently at the inner bank and out bank regions comply with Blanckaert et al. (2012).

4.3 Effect of *Re*

The effect of *Re* was investigated for Cases 1, 2, and 3. The only difference of these cases was the mean velocity. The *Re* values for the three cases were 23000, 30000, and 37000, respectively. In these cases, although similar patterns of secondary flow were found, the strength and size differed. The strength was quantified using the normalised streamwise vorticity component at the centre of the circulation cells. The characteristic length scale is defined as $L_c = \sqrt{(B_c/B) \times (H_c/H)}$ to represent the size of the circulation cells, where H_c and B_c are the height and width of circulation cells, respectively.

The variation in size and strength with *Re* in the 120° section are shown in Table 2. The increase in *Re* is followed by a decrease in both the strength and size of C1. The strength and size of C1 are reduced by 50%. With an increase in *Re*, the anisotropy of turbulence decreases, which indicates the diminished role of T_{ani}. In Case 3, the size of C1 is considerably smaller than that of S1. C1 is constrained to the outer bank region. Meanwhile, the size

Table 3 Variation of size and strength of the circulation cells with *B/H*.

Cases	B/H	L_c			$\lvert w_\theta H/U \rvert$		
		S1	S2	C1	S1	S2	C1
5	3.3	0.69	0.43	0.27	1.05	0.70	0.45
2	2.7	0.65	0.49	0.35	1.15	0.80	0.65
4	2	0.58	0.51	0.52	1.70	1.50	1.30

of S2 increases, whereas its strength decreases with the increase in *Re*. The increase in *Re* is often with the increase in *Fr*, which reflects the ratio of the inertial force to gravity. The enhanced inertial effect accounts for the expansion of the flow separation zone. The decreased strength of S2 also indicates that S2 belongs to turbulent-induced circulation. The size and strength of S1 do not change significantly when *Re* is large.

4.4 Effect of Aspect Ratio

The aspect ratio is an important dimensionless variable that influences secondary flow. The influences of *H/B* contain two components $H/B = (H/R)\cdot(R/B)$. In our experiments, $R/B = 3$ was constant. Many researches tried to relate strength of primary secondary flow with *H/R*, which represents the shallowness of the flow (Demuren & Rodi, 1986). The expression is in the form of $U_r^*/U \propto H/R$, where U_r^* denotes the cross-stream circulation velocity. This expression indicates that the circulation velocity has an increasing tendency with increasing *H/R*.

The effect of the aspect ratio was investigated with respect to Cases 5, 2, and 4. The only difference of these cases was the water depth. Table 3 shows the variation in the size and strength with *B/H* in the 120° section. The *B/H* values for the three cases are 3.3, 2.7, and 2.0, respectively. This is within the range of narrow natural rivers. The strengths of S1, S2, and C1 increase with a decrease in *B/H*, which is in agreement with previous research. The strengths of S1, S2, and C1 in Case 4 are almost twice as large as those in Case 5. The sizes of S2 and C1 are accordingly increase (owing to the enhancement effect of the side wall) with an increase in *H*. In narrow bends, the influence of the bank boundary layers is significant and is related to the formation of S2 and C1. Notably, the strength will not continue to increase with the increase in *H* owing to the complex interactions between secondary flow and streamwise velocity. **4.5 Experimental Error and Uncertainty Analyses**

During the velocity measurement process, the indicators that represent dada quality were guaranteed with signal-to-noise ratio larger than 20 dB. The uncertainty is defined as:

$$\varepsilon(f) = \frac{f_m - f_r}{f_r} \quad \text{.....(10)}$$

where f_m is the measured value, and f_r is the real value. The uncertainty of the time-averaged f is estimated using the standard error of the mean:

$$\varepsilon = \sigma_f / \sqrt{n} \quad \text{.....(11)}$$

where n represents the number of f-values, and σ_f represents the standard deviation. Based on the experimental data, an estimation of the uncertainty of experimental measurement data was made.

$$\varepsilon(u_\theta) \le 1\%, \varepsilon(u_r) \le 3\%, \varepsilon(u_z) \le 3\%, \varepsilon(u_i'u_j') \le 8\% \ldots \quad (12)$$

As the error shows slow space variation, Blanckaert and De Vriend (2004) proposed that:

$$\begin{aligned}\varepsilon(\partial f/\partial p) &= \frac{\partial\,(f_r + \varepsilon(f) f_r)/\partial p - \partial f_r/\partial p}{\partial f_r/\partial p} \\ &= \frac{\partial(\varepsilon(f) f_r)/\partial p}{\partial f_r/\partial p} < \frac{\varepsilon(f) f_r}{f_r} = \varepsilon(f)\end{aligned} \quad \text{.....(13)}$$

For two measured quantities p and q,

$$\begin{aligned}\varepsilon(pq) &= \frac{(p_r + \varepsilon(p)p_r)(q_r + \varepsilon(q)q_r) - p_r q_r}{p_r q_r} \\ &= \varepsilon(p) + \varepsilon(q) + \varepsilon(p)\varepsilon(q) \approx \varepsilon(p) + \varepsilon(q)\end{aligned} \quad \text{.....(14)}$$

Based on the error propagation theory, the uncertainty can be estimated：

$$\begin{aligned}
&\varepsilon(w_\theta) \le \varepsilon(v) + \varepsilon(w) = 6\% \\
&\varepsilon\left(-u_r\frac{\partial w_\theta}{\partial r} - u_z\frac{\partial w_\theta}{\partial z}\right) \le \varepsilon(u_r) + \varepsilon(u_z) + 2\varepsilon(w_\theta) = 16\% \\
&\varepsilon\left(\frac{u_r}{r}w_\theta\right) \le \varepsilon(u_r) + \varepsilon(w_\theta) = 7\% \\
&\varepsilon\left(\frac{\partial}{\partial z}\left(\frac{u_\theta^2}{r}\right)\right) \le 2\varepsilon(u_\theta) = 2\% \\
&\varepsilon\left(\frac{\partial}{\partial z}\left(\frac{\overline{u_\theta'^2}}{r}\right)\right) \le \varepsilon(u_\theta'^2) = 8\% \\
&\varepsilon\left(\frac{\partial^2}{\partial z \partial r}(\overline{u_r'^2} - \overline{u_z'^2}) + \frac{1}{r}\frac{\partial \overline{u_r'^2}}{\partial z}\right) \le \varepsilon(u_\theta'^2) + 2\varepsilon(u_r'^2) = 24\% \\
&\varepsilon\left(\frac{\partial^2 \overline{u_r'u_z'}}{\partial z^2} - \frac{\partial^2 \overline{u_r'u_z'}}{\partial r^2} - \frac{\partial}{\partial r}\left(\frac{\overline{u_r'u_z'}}{r}\right)\right) \le 3\varepsilon(\overline{u_r'u_z'}) = 24\%
\end{aligned} \quad (15)$$

Thus, according to Termini (2015), the experimental error and uncertainty will not affect the quantitative analysis.

5. CONCLUSIONS

Experiments were carried out to investigate the complex secondary flow pattern and the underlying mechanism of the multiple circulation cells in a narrow and sharp bend with $R/B = 3$ and $B/H < 5$. In contrast to wide and shallow rivers, in addition to the traditional bi-cellular pattern of cross-stream circulation, another circulation cell appeared in the vicinity of inner bank, which corresponds to the flow separation zone. Secondary

flow developed along the bend, and variations in secondary flow structures were due to the interactions of different flow processes. The underlying mechanism was explored by analysing the terms in streamwise vorticity equation. The convective transport, centrifugal force, and turbulence play leading roles in determining the patterns of secondary flow. T_{cf1} favoured S1 and C1 but opposed S2. T_{ani} and T_{rss} accounted for the formation of C1 and S2. T_{adv} maintained the existence of S2. The secondary flow pattern depends on the *Re* and aspect ratio. These two parameters reflect the turbulent and side wall effects. The circulation cells behaved differently with the variations in *Re* and aspect ratio, which reflects the different formation mechanisms of the circulation cells. C1 and S2 belong to turbulence-induced secondary flow, whereas S1 belongs to curvature-induced secondary flow. Since the turbulent characteristics play impotent roles in the generation of circulation cells, the extension may focus on the Reynolds stress distributions and kinetic energy fluxes from turbulent to time-averaged flow field. Farhadi et al. (2018) analysed the kinetic energy fluxes in the outer-bank zone, it is necessary to extend to the entire cross-section due to the unique secondary flow structure in narrow and sharp open-channel bends.

The secondary flow structure is practically relevant, which plays a significant part in sediment transport processes, especially involved in the suspended load. To predict the sediment transport and associated bathymetry evolution in curved channels, a 3D model is required to reflect the complex secondary flow structure. The depth-averaging process of 2D models makes it impossible to adequately account for the variation in circulation cells. The experiments were conducted in a flat bed, which can be considered as the initial situation of the erosion process. When the topography changes, the flow structure accordingly changes to maintain sediment transport equilibrium. Further research is required to explore the bed topography influences on the secondary flow structure in sharp bends. Field study provides the compelling findings; however, it is rarely difficult to alter case conditions for a thorough investigation of the curvature rate *R/B*. The variation of curvature ratio is not considered in out experiments. 3D numerical modelling provides another approach for investigating variable flow characteristics. The data obtained from our experiments can be used for model validation. Further investigations on the effect of *R/B* using CFD modelling are recommended for future research.

ACKNOWLEDGEMENTS

This study was funded by the National Natural Science Foundation of China (grant no. 11972265).

CONFLICT OF INTEREST

All authors have no conflicts to disclose.

AUTHORS CONTRIBUTION

All authors contributed to the study conception and design. Material preparation, data collection and analysis were performed by Peng Hu. The first draft of the manuscript was written by Peng Hu. Minghui Yu validated the results and reviewed the original draft of this paper.

REFERENCES

Abduo, S. S., Elmoustafa, A. M., & Salam, M. S. A. (2021). Study of counteracting the secondary flow in open channel bends. *Ain Shams Engineering Journal*, 12(3), 2425-2433. https://doi.org/10.1016/j.asej.2021.01.011.

Bathurst, J. C., Thorne, C. R., & Hey, R. D. (1977). Direct measurements of secondary currents in river bends. *Nature*, 269, 504–506. https://doi.org/10.1038/269504a0.

Bathurst, J. C., Hey, R. D., & Thorne, C. R. (1979). Secondary flow and shear stress at river bends. *Journal of the Hydraulics Division*, 105(10), 1277-1295. https://doi.org/10.1061/jyceaj.0005285.

Bai, Y. C., Song, X. L., & Gao, S. X. (2014). Efficient investigation on fully developed flow in a mildly curved 180° open-channel. *Journal of Hydroinformatics*, 16(6), 1250-1264. https://doi.org/https://doi.org/10.2166/hydro.2014.108.

Blanckaert, K., & De Vriend, H. J. (2004). Secondary flow in sharp open-channel bends. *Journal of Fluid Mechanics*, 498, 353-380. https://doi.org/https://doi.org/10.1017/S0022112003006979.

Blanckaert, K., & De Vriend, H. J. (2010). Meander dynamics: A nonlinear model without curvature restrictions for flow in open-channel bends. *Journal of Geophysical Research: Earth Surface* 115, F04011. https://doi.org/10.1029/2009JF001301.

Blanckaert, K. (2011). Hydrodynamic processes in sharp meander bends and their morphological implications, *Journal of Geophysical Research: Earth Surface* 116, F01003. https://doi.org/10.1029/2010JF001806

Blanckaert, K., Duarte, A., Chen, Q., & Schleiss, A. J. (2012). Flow processes near smooth and rough (concave) outer banks in curved open channels. *Journal of Geophysical Research: Earth Surface*, 117, F04020. https://doi.org/10.1029/2012JF002414.

Blanckaert, K. (2015). Flow separation at convex banks in open channels. *Journal of Fluid Mechanics*, 779, 432-467. https://doi.org/10.1017/jfm.2015.397.

Crosato, A. (2008). *Analysis and modelling of river meandering*. [PhD thesis, Delft University of Technology]. Delft, Netherlands.

Constantinescu, G., Koken, M., & Zeng, J. (2011). The structure of turbulent flow in an open channel bend of strong curvature with deformed bed: insight provided by detached eddy simulation. *Water Resources Research*, 47(5), *W05515*. https://doi.org/10.1029/2010WR010114.

Constantinescu, G., Kashyap, S., Tokyay, T., Rennie, C.

D., & Townsend, R. D. (2013). Hydrodynamic processes and sediment erosion mechanisms in an open channel bend of strong curvature with deformed bathymetry, *Journal of Geophysical Research: Earth Surface* 118, 480–496. https://doi.org/10.1002/jgrf.20042.

Demuren, A. O., & Rodi, W. (1986). Calculation of flow and pollutant dispersion in meandering channels. *Journal of Fluid Mechanics*, 172, 63–92. https://doi.org/10.1017/S0022112086001659.

Dey, S. (2014). *Fluvial hydrodynamics: hydrodynamic and sediment transport phenomena*. Springer, Berlin.

Dietrich, W. E., & Smith, J. D. (1983). Influence of the point bar on flow through curved channels. *Water Resources Research*, 19(5), 1173-1192. https://doi.org/10.1029/WR019i005p01173.

Feurich, R., & Olsen, N. (2011). Three-dimensional modeling of nonuniform sediment transport in an s-shaped channel. *Journal of Hydraulic Engineering*, 137(4), 493-495. https://doi.org/10.1061/(asce)hy.1943-7900.0000321.

Farhadi, A., Sindelar, C., Tritthart, M., Glas, M., Blanckaert, K., & Habersack, H. (2018). An investigation on the outer bank cell of secondary flow in channel bends. *Journal of Hydro-Environment Research*, 18, 1-11. https://doi.org/10.1016/j.jher.2017.10.004.

Hooke, R. B. (1975). Distribution of Sediment Transport and Shear Stress in a Meander Bend. *The Journal of Geology*, 88(5), 543-565. https://doi.org/10.1086/628140.

Hu, C., Yu, M., Wei, H., and Liu, C. (2019). The mechanisms of energy transformation in sharp open-channel bends: Analysis based on experiments in a laboratory flume. *Journal of Hydrology*, 571, 723-739. https://doi.org/10.1016/j.jhydrol.2019.01.074.

Johannesson, H., & Parker, G. (1989). Secondary flow in a mildly sinuous channel. *Journal of Hydraulic Engineering*, 115 (3), 289–308. https://doi.org/0.1061/(asce)0733-9429(1989)115:3(289).

Khosronejad, A., Rennie, C., Neyshabouri, S. & Townsend, R. D. (2007). 3D numerical modeling of flow and sediment transport in laboratory channel bends. *Journal of Hydraulic Engineering*, 133 (10), 1123–1134. https://doi.org/10.1061/(asce)0733-9429(2007)133:10 (1123).

Kashyap, S., Constantinescu, G., Rennie, C. D., Post, G., & Townsend, R. (2012). Influence of channel aspect ratio and curvature on flow, secondary circulation, and bed shear stress in a rectangular channel bend. *Journal of Hydraulic Engineering*, 128(12), 1045-1059. https://doi.org/10.1061/(asce)hy.1943-7900.0000643.

Kang, T., Kimura, I., & Shimizu, Y., (2018). Responses of bed morphology to vegetation growth and flood discharge at a sharp river bend. *Water*, 10(2):223. https://doi.org/10.3390/w10020223.

Luo J., & Razinsky, E. H. (2009) Analysis of turbulent flow in 180 deg turning ducts with and without guide vanes. *Journal of Turbomachinery*, 131,021011. https://doi.org/10.1115/1.2987239.

Mahmoodi, M., Nili-Ahmadabadi, M., Minaeian, A., Tavakoli, M. R., Norouzi, M., & Kim, K. C. (2021). Secondary flow structures in developing viscoelastic fluid flow through curved ducts with square cross section. *Meccanica*, 56, 2979-2999. https://doi.org/10.1007/s11012-021-01438-9.

Nanson, R. A. (2010). Flow fields in tightly curving meander bends of low width-depth ratio. Earth Surface Processes and Landforms: *The Journal of the British Geomorphological Research Group*, 35(2), 119-135. https://doi.org/10.1002/esp.1878.

Prandtl, L. (1942). *Führer durch die Strömungslehre*. Vieweg, Braunschweig.

Ruether, N., & Olsen, N. (2005). Three-dimensional modeling of sediment transport in a narrow 90° channel bend. *Journal of Hydraulic Engineering*, 131(10), 917-920. https://doi.org/10.1061/(asce)0733-9429(2005)131:10(917).

Russell, P., & Vennell, R. (2019). High Resolution Observations of an Outer-Bank Cell of Secondary Circulation in a Natural River Bend. *Journal of Hydraulic Engineering*, 145(5). 04019012. https://doi.org/10.1061/(asce)hy.1943-7900.0001584.

Stoesser, T., Ruether, N., & Olsen, N. R. B. (2010). Calculation of primary and secondary flow and boundary shear stresses in a meandering channel. *Advances in Water Resources*, 33(2), 158-170. https://doi.org/10.1016/j.advwatres.2009.11.001.

Thomson, J. (1876). On the origin of windings of rivers in alluvial plains, with remarks on the flow of water round bends in pipes. *Proceedings of the Royal Society of London*, 25, 5–8. https://doi.org/10.1098/rspl.1876.0004.

Termini, D. (2015). Momentum transport and bed shear stress distribution in a meandering bend: Experimental analysis in a laboratory flume. *Advances in Water Resources*, 81,128-141. https://doi.org/10.1016/j.advwatres.2015.01.005.

Van Balen, W., Uijttewaal, W. S., & Blanckaert, K. (2009). Large-eddy simulation of a mildly curved open-channel flow. *Journal of Fluid Mechanics*, 630, 413-442. https://doi.org/10.1017/S0022112009007277.

Van Balen, W., Blanckaert, K., & Uijttewaal, W. S. (2010). Analysis of the role of turbulence in curved open-channel flow at different water depths by means of experiments, LES and RANS. *Journal of Turbulence*, 11, N12. https://doi.org/10.1080/14685241003789404.

Vaghefi, M., Akbari, M., & Fiouz, A. R. (2016). An

experimental study of mean and turbulent flow in a 180 degree sharp open channel bend: Secondary flow and bed shear stress. *KSCE Journal of Civil Engineering*, 20, 1582-1593. https://doi.org/https://doi.org/10.1007/s12205-015-1560-0

Wei, M., Blanckaert, K., Heyman, J., Li, D., & Schleiss, A. J. (2016). A parametrical study on secondary flow in sharp open-channel bends: experiments and theoretical modelling. *Journal of hydro-environment research*, 13, 1-13. https://doi.org/10.1016/j.jher.2016.04.001.

Yan, X., Rennie, C. D., & Mohammadian, A. (2020). A three-dimensional numerical study of flow characteristics in strongly curved channel bends with different side slopes. *Environmental Fluid Mechanics*, 20, 1491-1510. https://doi.org/10.1007/s10652-020-09751-9.